



# Fabrication, characterization, and in vitro bioactivity evaluation of freeze-cast highly porous hardystonite ceramic reinforced by graphene oxide as a novel bone scaffold

Mojdeh Azizi<sup>1</sup> · Mahdi Kalantar<sup>1</sup> · Nader Nezafati<sup>2</sup> · Ali Zamanian<sup>2</sup>

Received: 18 November 2020 / Revised: 27 March 2021 / Accepted: 4 April 2021 / Published online: 10 April 2021  
© Australian Ceramic Society 2021

## Abstract

One of the major challenges in bone tissue engineering is the preparation of highly interconnected porous scaffolds with suitable mechanical properties. Synthetic scaffolds used in medicine are usually made of single-phase of ceramic or polymer. However, the combination of these materials with graphene-based nanofillers can produce scaffolds with improved mechanical and biological properties. In this research, we synthesize highly porous (up to 85%) and lamellar hardystonite-graphene oxide (0–1.5 wt% GO) composite scaffolds through the freeze-casting technique and then sintering it for 5 h at 1150 °C. The results of microstructural observations showed using higher amounts of GO leads to an increase in the porosity and a decrease in the shrinkage level. The optimum mechanical properties among the studied samples are related to HT-1 wt% GO ( $E = 71.77 \pm 2.40$  MPa,  $\sigma = 1.8 \pm 0.16$  MPa, and  $K = 47.87$  MJ/m<sup>3</sup>). Therefore, biological tests were performed on the HT-1 wt% GO scaffold and HT scaffold as the optimal and control samples, respectively. In vitro bioactivity experiments confirm the formation of apatite on surfaces of HT and HT-1 wt% GO specimens after soaking them in SBF for 14 days in static circumstances. Based on the cell studies, the HT-1 wt% GO scaffold sample showed the best attachment and proliferation of osteoblastic cells. The methyl thiazole tetrazolium (MTT) assays were used to characterize the biocompatibility of the HT-1 wt% GO composites in vitro. Also, the alkaline phosphatase (ALP) activity and proliferation rate of cells on the HT-1 wt% GO composite was higher compared with the pure HT ceramics. Overall, it is concluded that the HT-1 wt% GO scaffold with enhanced biological and mechanical features is suitable for use as a novel bone scaffold.

**Keywords** Graphene oxide · Hardystonite · Bone scaffolds · Freeze-casting · Mechanical and biological properties

## Highlights

- Hardystonite (HT) scaffolds with different contents of (0, 0.5, 1, and 1.5 wt%) graphene oxide (GO) were successfully fabricated by freeze-casting method.
- Investigation of microstructure, physical, and mechanical properties of scaffold samples with different weight ratios of GO.
- Investigation of biological properties on the HT-1 wt% GO scaffold as the optimal sample and HT scaffold as the control sample.
- The HT-1 wt% GO scaffold with improved mechanical and biological properties could have a potential to be used as a novel bone scaffold.

✉ Mahdi Kalantar  
mkalantar@yazd.ac.ir

<sup>1</sup> Materials Engineering Group, Department of Mining and Metallurgical Engineering, Yazd University, Yazd 89195-741, Iran

<sup>2</sup> Biomaterials Research Group, Department of Nanotechnology and Advanced Materials, Materials and Energy Research Center, Karaj 3177983634, Iran

## Introduction

The development of novel biomaterials with high biocompatibility and high bone restoration or bone formation capability in the human body has been the subject of intense research in bone engineering [1, 2]. In this regard, the fabrication of tridimensional scaffolds—regarding their high porosity, optimal mechanical strength, excellent cell attachment, and anisotropic structures—is one of the priorities in tissue engineering [3]. The freeze-casting technique has been widely used in recent years for fabricating anisotropic porous materials. For this purpose, materials with different shapes including nanoparticles, nanotubes, nanofibers, and nanosheets (graphene derivatives) are used. These materials can be stably dispersed and have novel properties and a wide range of applications [4–13]. This technique involves freezing a solution or suspension and then sublimation of ice crystals to vapor at low pressure and subsequent densification by post-treatment of the porous

sample. The result is a tridimensional scaffold with an anisotropic porous structure [13–18].

In recent decades, the fabrication and use of calcium silicate scaffolds such as hardystonite ceramic ( $\text{Ca}_2\text{ZnSi}_2\text{O}_7$ ) have been highly considered in the field of ceramic biomaterials. This high interest is attributed to the superior biological features like high bioactivity, the good ability for the absorption of biological agents, good biocompatibility, cellular responses, and especially higher mechanical properties of these scaffolds compared to calcium phosphate scaffolds [19]. The simultaneous presence of elements such as silicon, calcium, and zinc in hardystonite ceramic leads to antibacterial activity and a good proliferation of osteoblast cells, resulting in a good metabolism and osteogenesis [20–22].

Graphene has been recently the subject of intense research because of the exceptional thermal, electrical, and mechanical features [23, 24]. Regarding good biocompatibility, extremely large surface area, biostability, and chemical functionalization of graphene, it is used as an agent for strengthening and toughening in composite materials. Therefore, it can be used in different biocomposites as a scaffold in bone tissue engineering. Most studies on graphene composites focus on polymer matrix composites [25–29]. Today, a growing interest is witnessed in using graphene-based nanofillers like graphene oxide (GO), graphene nanoplatelets (GNPs), and reduced graphene oxide (rGO) for enhancing the biological and mechanical properties of bioceramics and ceramics like  $\text{Si}_3\text{N}_4$  [30, 31],  $\text{Al}_2\text{O}_3$  [32], hydroxyapatite (HA) [33, 34], bioactive glasses [35, 36], and calcium silicate ( $\text{CaSiO}_3$ ) [37]. All ceramic matrix composites reinforced by graphene show a tendency for increasing fracture toughness, mostly because of crack deflection, crack bridging, crack branching, and crack-tip shielding. In this regard, pristine graphene nanosheets are hydrophobic and tend to form agglomerates. Meanwhile, the existence of abundant hydroxyl, epoxy, and carbonyl groups on the GO basal plane can promote interfacial interactions. Furthermore, good biocompatibility and high hydrophilicity of GO sheets indicate that GO could be a promising and ideal nanoscale reinforcement filler in biocomposites for interfacial bonding improvement of the composites and their bioactivity [38].

As mentioned before, graphene oxide has unique properties in tissue engineering and the freeze-casting technique. Hence, different graphene oxide-hardystonite composite scaffolds were produced with high porosity, good mechanical strength for the lowest possible solid loading, and biological properties for the objective of applicability in bone tissue engineering. To this aim, the sol-gel technique was used to synthesize the nanostructure-hardystonite powder, and then, the lamellar GO/HT composite scaffolds were fabricated by freeze-casting. The microstructural observations, phase analysis, mechanical features, and cell performance of the scaffold were performed to evaluate the potential of the scaffold for use in tissue engineering.

## Materials and methods

### Materials

Tetraethyl orthosilicate (TEOS) ( $\text{Si}(\text{OC}_2\text{H}_5)_4$ , Merck, 800658), calcium nitrate tetrahydrate ( $\text{Ca}(\text{NO}_3)_2 \cdot 4\text{H}_2\text{O}$ , Merck, 2069), zinc nitrate hexahydrate ( $\text{Zn}(\text{NO}_3)_2 \cdot 6\text{H}_2\text{O}$ , Merck, 10196-18-6), nitric acid ( $\text{HNO}_3$ , Merck, 1.00456.2500), Dolapix as a dispersant (Dolapix CA 64, Zchimmer and Schwarz), polyvinyl alcohol (PVA) (Fluka, 81384), and single-layer graphene oxide dispersion in water (Kara Pajuhesh Amirkabir company, Iran, the concentration of 5mg/ml, single layer ratio > 80%, the lateral size of 0.5–2  $\mu\text{m}$ , and thickness of 0.5–1 nm for sheets of graphene oxide, pH = 4) were utilized for the synthesis of HT powder and HT/GO scaffold.

### Synthesis of hardystonite nanopowder

The sol-gel process was used to synthesize hardystonite powders. For this purpose, calcium nitrate tetrahydrate ( $\text{Ca}(\text{NO}_3)_2 \cdot 4\text{H}_2\text{O}$ ), tetraethyl orthosilicate ( $(\text{C}_2\text{H}_5\text{O})_4\text{Si}$ ), and TEOS and zinc nitrate hexahydrate ( $\text{Zn}(\text{NO}_3)_2 \cdot 6\text{H}_2\text{O}$ ) were used as raw materials. The TEOS was dissolved in a solution of water and 2M  $\text{HNO}_3$  (molar ratio of  $\text{TEOS}/\text{H}_2\text{O}/\text{HNO}_3 = 1:8:0.16$ ) and hydrolyzing was performed for 30 min while stirring. The  $\text{Ca}(\text{NO}_3)_2 \cdot 4\text{H}_2\text{O}$  and  $\text{Zn}(\text{NO}_3)_2 \cdot 6\text{H}_2\text{O}$  were inserted into the created TEOS solution (molar ratio of  $\text{TEOS}/\text{Zn}(\text{NO}_3)_2 \cdot 6\text{H}_2\text{O}/\text{Ca}(\text{NO}_3)_2 \cdot 4\text{H}_2\text{O} = 2:1:2$ ). To complete the hydrolysis reaction, stirring the reactants was performed for 5 h at room temperature. Then, the prepared solution was kept at 60 °C for a day and dried for 2 days at 120 °C to achieve the dry gel. Then, the dry gel was ground and sieved using a #250 mesh, and then, it was transferred into a corundum crucible. Calcination was performed for 3 h at 1150 °C (a heating rate of 5 min/°C). A planetary ball mill was used to ground the calcined powder (Retsch, PM400, with zirconia ball to powder ratio of 10 for 6 h with 300 rpm).

### Preparation of HT/GO suspension

To prepare a suspension of hardystonite/oxide, the calcined hardystonite powder and graphene oxide were mixed at different weight ratios of graphene oxide (0, 0.5, 1, 1.5) (Table 1) and were dispersed in deionized water (volume ratio of 7.5%)

**Table 1** Summary of all data calculated from XRD data by the Williamson-Hall method (the crystallite size  $D$  and strain  $\epsilon$ )

Sample	Slope	Intercept	$\epsilon$	$D$ (nm)
Hardystonite	– 0.0002	0.0216	– 0.0002	46.3

in the presence of dispersant (4 wt% Dolapix) and binder (4 wt% PVA). Every composition was stirred for almost 20 min to obtain a homogenous suspension. Next, it was degassed in a vacuum desiccator for about 15 min.

### Scaffold fabrication

A custom-made setup was used to prepare the scaffolds as previously described [7]. Briefly, the obtained suspensions of HT-GO were poured into a polytetrafluoroethylene (PTFE) mold with a 2-cm internal diameter and placed in a freeze-cast system containing a cold copper plate equipped with liquid nitrogen, a thermocouple, and a PID controller. The slurries were frozen at a cooling rate of 1 min/°C. The freeze-cast specimens were put in a freeze dryer (FD-10, Pishtaz Engineering Co., Tehran, Iran) at a vacuum pressure of 0.5 Torr and – 58 °C for 72 h to redirect the ice crystals. The green bodies were sintered in an argon atmosphere in an electric furnace according to a three-stage thermal program and soaking time of (1) 1 h up to 300 °C with the rate of 2 °C per min, (2) up to 600 °C (2 °C per min, 1 h), and (3) 1150 °C (2 °C/min, 5 h).

### Characterization

The Raman scattering of graphene oxide sheets was obtained by using a dispersive Raman microscope (Bruker, Senterra, excitation at 785 nm, laser power of 25 mW, spectral range of 400–3000 cm<sup>-1</sup>). The optimum temperature for calcinating the hardystonite powder was determined through thermal analysis on the dry gel including thermogravimetry (TG) and differential thermal analysis (DTA). The tests were performed using a thermo-analyzer (BÄHR, model STA 504, Germany) in the argon atmosphere, and the heating rate of 10 °C/min.

Phase and microstructural study of the samples were conducted using an X-ray diffractometer (Philips Co., PW1730, Netherlands, 40 kV, 30 mA, λ<sub>Cu-Kα</sub> = 1.54 Å, 20° ≤ 2θ ≤ 80°, and the scan speed of 1°/s). Next, the crystallite sizes (*D*<sub>XRD</sub>) and microstrain (ε) of the calcined powder were determined via the X’Pert High Score and the model was suggested by Williamson and Hall [39] (Eq. (1)).

$$\beta \cos\theta/\lambda = k/D_{XRD} + 4 \varepsilon \sin\theta/\lambda \tag{1}$$

where β is the width of the diffraction peak after subtraction of the instrumental effects, which is regarded as the summation of widths caused by the small crystallite sizes and lattice strains, λ denotes the applied wavelength of the X-rays, θ is the Bragg angle, *D*<sub>XRD</sub> is the mean crystallite size determined in a direction vertical to the surface of the specimen, ε is the lattice strain, and *k* is a constant dependent on the crystal structure.

The scanning electron microscopy (SEM; Stereo scan S 360-Leica Cambridge model) was utilized to characterize the morphology of the synthesized hardystonite powder and the morphological and microstructural study of HT/GO scaffolds.

To study the functional groups in the synthesized hardystonite and fabricated composite scaffold samples, 10 mg of the desired powder was combined with 800 mg of KBr and pressed into a transparent KBr pellet. Fourier transform infrared spectroscopy (FTIR) analysis was carried out in the frequency range of 4000–400 cm<sup>-1</sup> (a resolution of 2 cm<sup>-1</sup>) using the BRUKER VECTOR infrared spectrometer.

The compressive strength of sintered scaffold samples was measured using the machine of Santam (model STM-20, Iran) with a height of ~ 20 mm, a diameter of ~ 15 mm, and a crosshead speed of 5 mm/min. The uniaxial compressive stress (σ), Young’s modulus (*E*), and toughness (*K*) data were calculated from the stress-strain curve of the compressive test.

A gas pycnometer was used to calculate the actual density of HT and HT/GO composite powders.

The percentage of overall porosity (*P*) of sintered scaffolds was determined via Eq. (2) [40].

$$P = 1 - \frac{\rho_{Scaffold}}{\rho_{Solid}} * 100 \tag{2}$$

The sample’s volume before and after sintering was used to determine the shrinkage volume of sintered samples, as follows [41]:

$$S_V = (V_0 - V_f) / V_0 \tag{3}$$

The ability of apatite formation on the surface of prepared scaffolds was assessed by soaking the sintered scaffolds in simulated body fluid (SBF) at solid to liquid (S to L) loading of 1/100 (g/ml) and then maintained for 14 days at 37 °C. The SBF with a pH of 7.2 to 7.4 was bought from Aprin Advanced Technologies Development Company (Tehran, Iran) prepared based on the procedure proposed by Kokubo et al. [42]. The morphological and microstructure evaluation of the samples was done using FESEM (TESCAN Model MIRA3 XMU) equipped with the EDS-mapping system. The phase analysis for the specimens after soaking for 14 days in SBF was also assessed by XRD.

To evaluate the biodegradability of the samples after exposure to the aqueous medium, the weight loss of the samples after soaking in the phosphate-buffered saline (PBS) solution was determined. For this purpose, the PBS solution was first prepared by dissolving one PBS tablet in 100 ml of deionized water, and then, samples were prepared in tablet form and weighed after drying at room temperature. Each sample was then placed in 50 ml of solution for different time intervals. At the end of each interval, the specimen was rinsed with distilled water and dried at room temperature. Finally, the degradability rate of samples over time was measured by Eq. (4):

$$\Delta W = 100 \left( \frac{W_d - W_s}{W_d} \right) \quad (4)$$

where  $\Delta W$  is the weight loss percentage,  $W_d$  is the weight of the dried specimen, and  $W_s$  is the dried sample weight after immersion in PBS solution.

Before the extraction test, samples were sterilized for 30 min with UV according to ISO 10993-5. For each 0.2 g sample, 1 ml of the culture medium was used. Here, the initial cellular tests (MTT, ALP, cell adhesion) were conducted to assess the scaffolds' biological properties.

MTT (3-(4,5-dimethylthiazol-2-yl)-2,5-diphenyltetrazolium bromide) assay was used to calculate the cell viability of HT and HT-1GO samples at the predefined duration of 1, 3, and 7 days. Dulbecco's Modified Media (DMEM) were used to culture normal human osteoblast cells; then, incubation was performed in a humidified atmosphere of 5% CO<sub>2</sub> at 37 °C. MG63 osteoblast cells were planted at a density of 50,000 cells/well in 96-well plates, and incubation was performed for 24 h. Cell survival was defined by adding 15  $\mu$ l of MTT solution (5 mg/ml) to every well after further incubation for 4 h at 37 °C. The absorbance of the isopropanol-solubilized blue-colored solution (formazan) was determined at 570 nm using a photospectrometry plate reader (Tescan Elisa) and the percent viability of the cell was estimated compared to the control untreated cells. Finally, Eqs. (5) and (6) were used to determine the viability of the samples and compare the samples with each other [43].

$$\text{Toxicity}\% = \left( 1 - \frac{\text{Mean OD of sample}}{\text{Mean OD of control}} \right) * 100 \quad (5)$$

$$\text{Viability}\% = 100 - \text{Toxicity}\% \quad (6)$$

To evaluate alkaline phosphatase (ALP) activity, MG63 osteoblast cells were planted (100,000 cells/disc) onto the specimens (0.5 mm  $\times$  20 mm) and incubation was conducted

for 10 days. Next, the culture medium was eliminated from the plate wells and the scaffolds containing MG63 osteoblast cells were washed twice with PBS and 400  $\mu$ l of liquid pNPP and, finally, added to the cells on the scaffold. An assay was used to measure quantitative ALP activity through the hydrolysis of a colorless phosphate ester precursor (PNPP, p-nitrophenyl phosphate) into a yellow substance (p-nitrophenyl and phosphate). They were incubated for 30 min to yield a yellow-colored solution. The reaction was stopped by adding 100  $\mu$ l of NaOH (N2) solution and then the absorbance was recorded at 405 nm through a spectrophotometer microplate reader (Molecular Devices, Sunnyvale, CA).

About 100,000 MG63 osteoblast cells were cultured on HT and HT-1% GO for cell adhesion. After 72 h, the cells were fixed with 4% glutaraldehyde for 3 h. Then, the specimens were rinsed with PBS and dehydrated with some graded ethanol/water solutions (50–90% and 2  $\times$  100%, respectively). Samples were immersed individually in each solution for 30 min. After drying, the samples were examined by SEM to evaluate cell morphology.

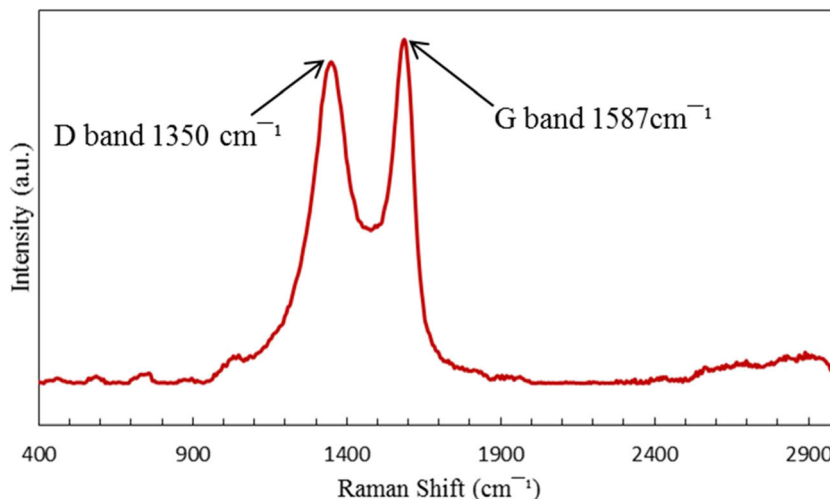
Tukey test and one-way ANOVA were conducted for the data with a significance level of  $p < 0.05$ . Also, data processing was conducted through Microsoft Excel 2013 software and the outcomes were expressed as a mean  $\pm$  standard deviation of at least 5 tests.

## Results and discussion

### Powder characterization

Graphene oxide material was characterized from its Raman scattering (Fig. 1), which typically exhibits two characteristic peaks, the G band at 1587 cm<sup>-1</sup> and the D band at 1350 cm<sup>-1</sup> arising from the in-plane sp<sup>2</sup> carbon-carbon bond stretching

Fig. 1 Raman spectrum of GO



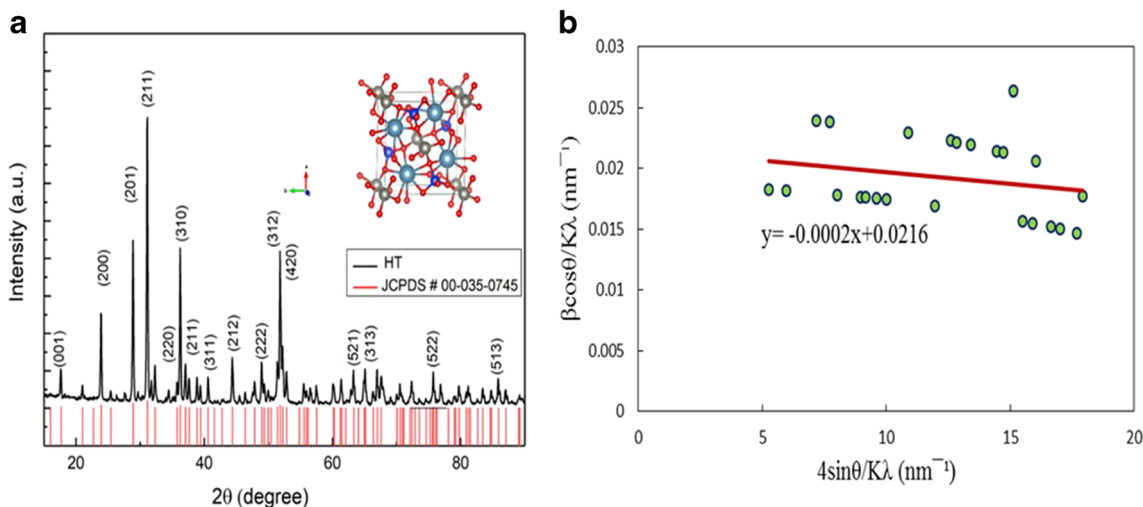


**Fig. 2** **a** XRD pattern. **b** Williamson-Hall plot of hardystonite powder. The strain is extracted from slope and crystallite size is extracted from *y*-intercept of fit

motion (symmetric  $E_{2g}$  mode) and the  $A_{1g}$  mode induced by disorders and edges, respectively. The results confirm that the graphene oxide is single layer [44].

The XRD pattern of synthesized hardystonite powder calcined at 1150 °C (Fig. 2a) confirms the formation of the hardystonite pure phase (JCPDS00-035-0745). According to data calculated based on the Williamson-Hall model (Fig. 2b, Table 1), the average size of hardystonite crystallite is in the nanoscale domain (46.3 nm). Thus, owing to the synthesis technique and low calcination temperature, the obtained crystallite size was finer than that reported by previous investigations [45, 46].

The DTA and TG curves of the as-dried hardystonite gel (Fig. 3a) indicate a weight loss of almost 35% within the range 450–650 °C. Also, the DTA curve shows two endothermic peaks at 550 and 650 °C due to decomposing the nitrates and organic precursors, respectively, and condensing the silanol groups. The existence of a broad and small exothermic peak at about 800 °C can be due to the crystallization of the

glassy phase [47, 48]. One exothermic peak was observed at 1150 °C, which corresponds to the formation of the hardystonite compound. Besides, an endothermic peak was observed around 1160 °C, which is attributed to the melting point ( $T_m$ ) of hardystonite [49]. For this reason, the calcination temperature of synthesized hardystonite powder was lower than 1160 °C (1150 °C, 3 h) due to the remaining nitrate and organic agents.

According to the FTIR results for the hardystonite sample (Fig. 3b), two peaks appear at 455  $cm^{-1}$  and 499  $cm^{-1}$  associated with the Ca-O and Zn-O functional groups and some other peaks appear at 617, 681, 835, 911, 970, and 1010  $cm^{-1}$  related to the  $SiO_4$  groups [49]. For the hardystonite-graphene oxide composite sample, in addition to hardystonite absorption peaks, some peaks corresponding to graphene oxide appear. Moreover, the curve shows a wide peak at 3400  $cm^{-1}$  for the hydroxyl group's O-H bond, a C=O bond of the carboxyl group at 1734  $cm^{-1}$ , a C=C bond of unoxidized graphite  $sp^2$  at 1627  $cm^{-1}$ , and epoxy group C-O-C bond and carbonyl group

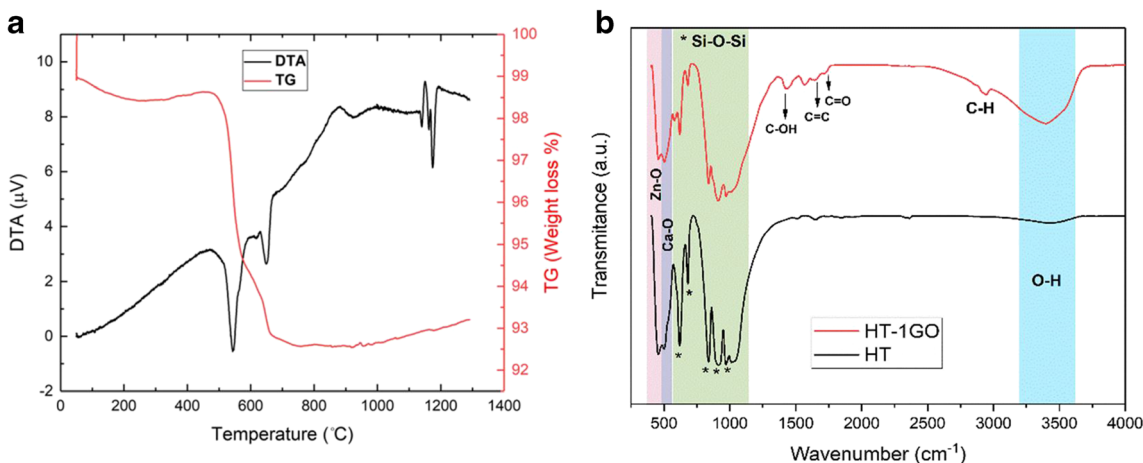


**Fig. 3** **a** STA curve of hardystonite dry gel up to the temperature of 1300 °C in the atmosphere of Ar and heating rate of 10 °C/min. **b** FTIR spectra of the HT and HT-1GO scaffolds prepared by freeze-cast method

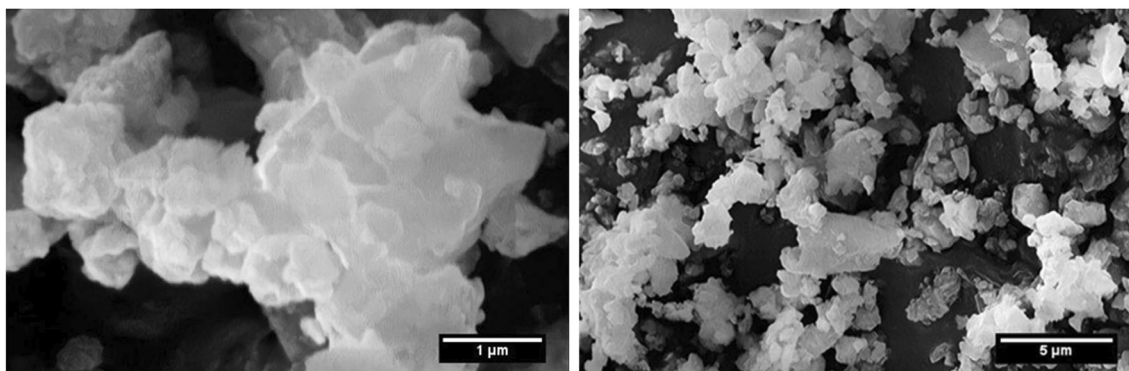


**Fig. 4** SEM photographs of microstructures of the hardystonite powders calcined at 1150 °C for 3 h at a heating rate of 5 min/°C

C-O bond below  $1250\text{ cm}^{-1}$ . The existence of such oxygen groups in the graphene oxide structure reveals the oxidation and degradation of the graphite structure with the  $sp^2$  area and its replacement with the  $sp^3$  oxide regions [50–52].

The SEM image of the synthesized powders in Fig. 4 indicates a porous and relatively agglomerated structure. The particle size of 500 nm is obtained by an image analyzer ( $n = 50$ ), which is consistent with the previous investigations [52–55].

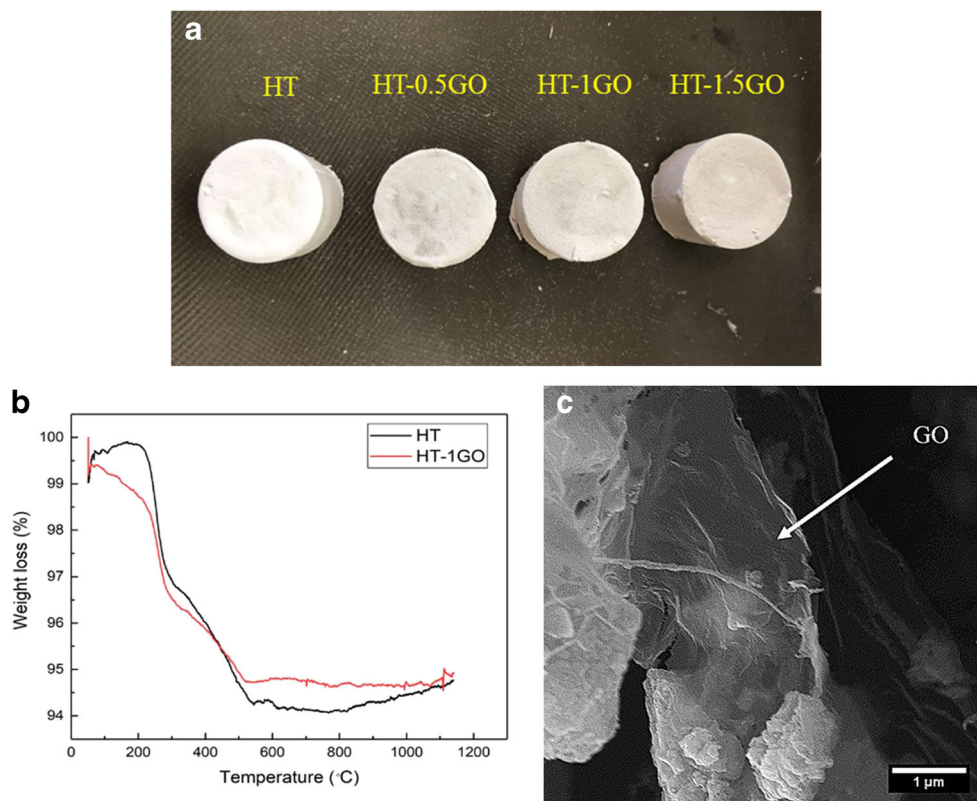
### Scaffold characterization

Figure 5 a shows scaffolds fabricated by freeze-casting method with various contents (0, 0.5, 1, and 1.5 wt%) of graphene oxide (GO). To investigate the thermal degradation of graphene oxide

in composite scaffold samples at high temperatures, two freeze-dried scaffold samples of HT and HT-1GO were subjected to thermal analysis with argon medium and at a temperature of 1150 °C and a heating rate of 10 °C/min (Fig. 5b). Primary weight loss in both samples is related to water evaporation, the secondary weight loss at 230 °C is attributed to PVA burning, and the third weight loss that occurs in the temperature range of 230 to 570 °C is related to Dolapix decomposition in the structure [56, 57]. Therefore, graphene oxide is not degraded in the argon medium. Also, the FESEM image of the sintered HT-1GO scaffold sample (Fig. 5c) demonstrates graphene oxide plates in the structure [58, 59].

The SEM micrographs of the horizontal and vertical cross sections of scaffold samples for different weight

**Fig. 5** **a** Fabricated scaffolds by freeze-casting method with different contents (0, 0.5, 1, and 1.5 wt%) of graphene oxide (GO). **b** TGA curves of the HT and HT-1GO scaffolds before sintering. **c** FESEM of sintered HT-1GO scaffold sample



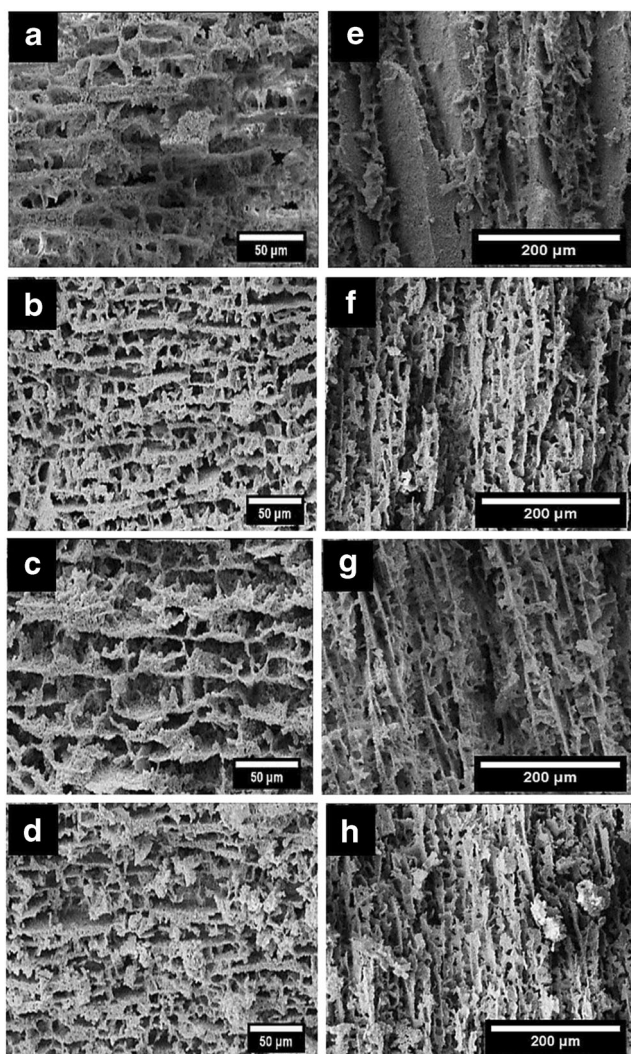


**Fig. 6** Horizontal **a** HT, **b** HT-0.5GO, **c** HT-1GO, and **d** HT-1.5GO and vertical **e** HT, **f** HT-0.5GO, **g** HT-1GO, and **h** HT-1.5GO cross-sectional SEM micrographs of scaffolds by different weight ratios of GO

ratios of GO (Fig. 6) show a lamellar microstructure of HT/GO plates in the freeze-cast stage of fabrication followed by freeze-drying with their flat interconnected macropores in the ice growth direction. Due to the

presence of PVA [60] or entrapped particles in ice [61], a branch-like dendritic structure and ceramic bridges linking nearby ceramic plates are seen on the internal walls of the layers [60]. By increasing the GO quantity to 1.5 wt% in the composite, high interconnected porosity, and well-defined pores were observed in the SEM images [4, 62]. No significant differences were observed between the pore size of HT/GO and HT scaffolds such that the average pore size was in the range of 90–150 μm. So, because of the advantages of proliferation and cell attachment, cell ingrowth is possible [63].

The mechanical features of sintered scaffolds were characterized by compressive tests (Table 2, Fig. 7). It can be seen that the compressive strength first increased from  $0.78 \pm 0.02$  MPa for HT to  $1.48 \pm 0.04$  MPa and  $1.8 \pm 0.16$  MPa for HT-0.5GO and HT-1GO, respectively. Then, it decreased to  $0.73 \pm 0.01$  MPa for the HT-1.5GO sample. The elastic modulus of scaffolds also increased by increasing the graphene oxide up to 1 wt%. This increase can be related to the high specific surface area, better interfacial bonding, and 2D geometry of GO that tends to tangle and agglomerate. The reduction of mechanical properties for the HT-1.5GO sample can be attributed to the higher porosity of the sample in 1.5 wt% GO [37]. The addition of 1 wt% of graphene oxide improved the toughness of HT from  $16.94$  to  $47.87$  MJ/m<sup>3</sup> by reinforcing mechanism (bridge) and efficient energy dissipation [64, 65]. The data of the HT-1GO scaffold showed that the highest compressive strength and fracture toughness among the tested samples. Meanwhile, the reduced increase in the strength of HT-1.5GO might be attributed to the degradation in the dispersion of graphene at high content [66]. The good distribution of GO in the grain boundaries of the ceramic matrix impeded the migration of grain boundaries during the sintering of the composite sample, leading to the formation of fine microstructures with smaller defect sizes [67, 68]. The results of the obtained mechanical properties from HT-1.5GO show a significant improvement in mechanical properties with the higher porosity compared to previous researches using the freeze-casting method [69–71].

**Table 2** Experimental data of physical and mechanical properties of HT/GO scaffolds

Sample	Physical properties		Mechanical properties		
	Volume shrinkage (%)	Porosity (%)	Compressive strength (MPa)	Young’s modulus (MPa)	Toughness (MJ/m <sup>3</sup> )
HT	$40.78 \pm 1.15$	$84.05 \pm 1.45$	$0.78 \pm 0.02$	$3.75 \pm 0.45$	16.94
HT-0.5GO	$40.62 \pm 1.02$	$85.5 \pm 0.93$	$1.48 \pm 0.04$	$51.23 \pm 4.75$	17.50
HT-1GO	$36.44 \pm 0.86$	$89.7 \pm 1.24$	$1.8 \pm 0.16$	$71.77 \pm 2.40$	47.87
HT-1.5GO	$35.95 \pm 1.23$	$90.07 \pm 1.43$	$0.73 \pm 0.01$	$53.74 \pm 6.88$	7.89

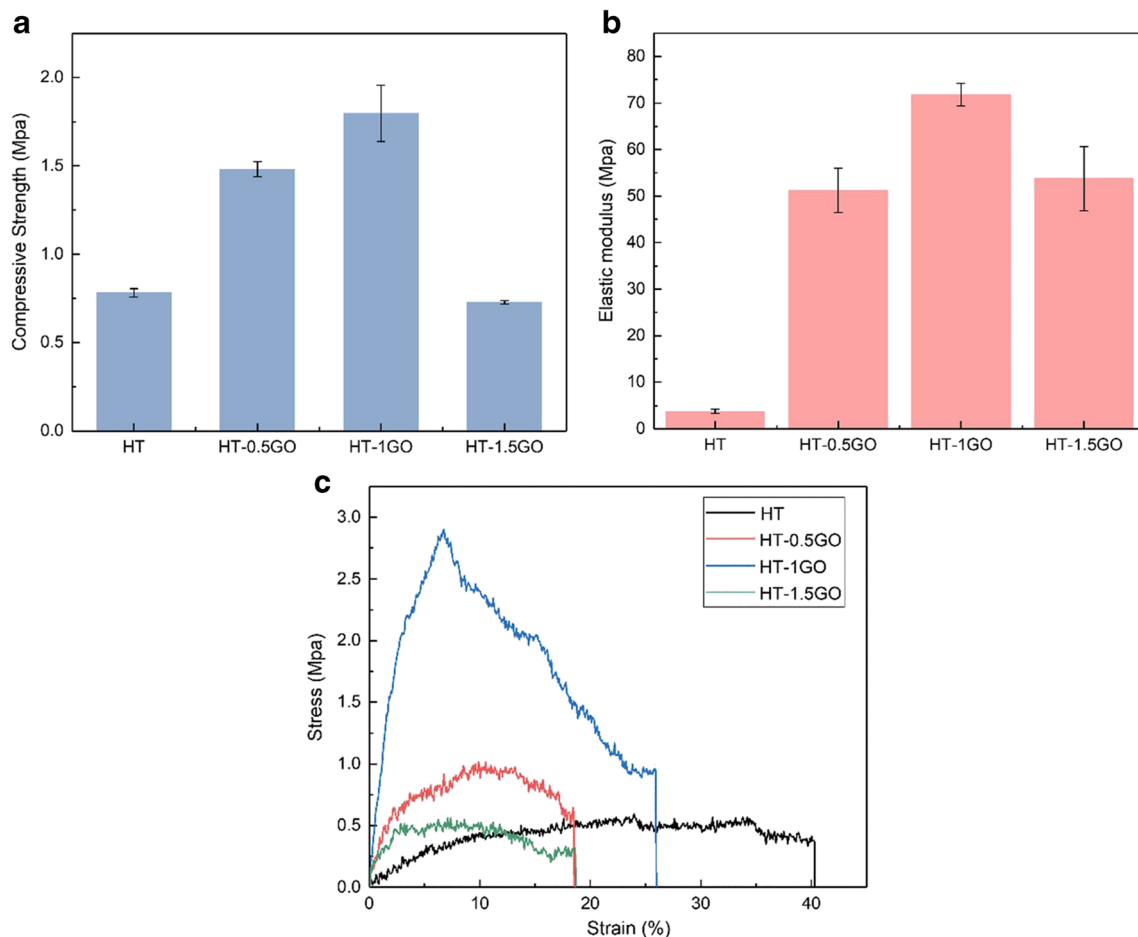


**Fig. 7** Evaluation of mechanical strength of the composite scaffolds (a), compressive strength (b), and elastic modulus (c) stress-strain graph (by compression testing)

The total porosity in the freeze-casting method depends on various parameters in the fabrication process of scaffolds like the solvent nature and its surface tension, viscosity, morphology, particle size distribution, the existence of different additives in the suspension [72], and freezing temperature. According to Table 2, for the sample with a higher content of GO, the porosity is slightly higher and the volume shrinkage is lower, probably due to the separation of grains and preventing pore closure by graphene oxide [73].

### Biological evaluation

Figure 8 shows the FESEM micrographs and elemental mapping of HT and HT-1GO scaffolds followed by soaking in the SBF solution for 14 days under static conditions. The elements discovered in the particles are the same as those of hydroxyapatite. As previously mentioned, scaffolds containing GO form more hydroxyapatite over the scaffold's surface [74]. Carboxyl groups of GO with a negative charge facilitate the formation of hydroxyapatite via interaction with  $\text{Ca}^{2+}$ , i.e., the fundamental cation of the hydroxyapatite composition, and then hydroxyapatite formation with  $\text{PO}_2^{3-}$  [75]. On the

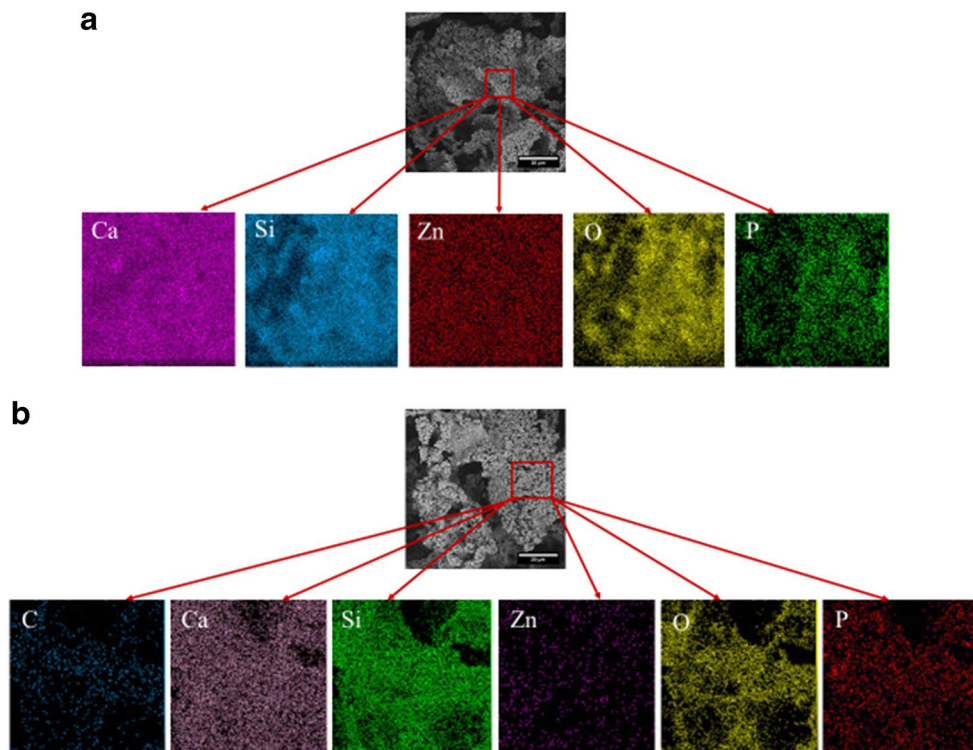
surface of both samples, the precipitate formed during the soaking in the SBF solution is observed. Also, the XRD analysis confirms the presence of hydroxyapatite (JCPDS00-009-0432) in the mentioned precipitate (Fig. 9). The capability to create apatite on hardystonite ceramics was not influenced negatively by incorporating graphene oxide for the HT-1GO scaffold sample. Besides, the XRD analysis shows a strong and large peak indicating the high formation of nanocrystalline HA.

Figure 10 a presents the weight loss changes of HT and HT-1GO scaffolds after immersion for 21 days in the PBS solution. Based on the obtained result, the weight loss changes of the HT sample in the early days was higher than the HT-1GO sample, indicating the lower mechanical strength of the HT sample compared to the composite specimen. After 7 days, the composite sample indicates more weight loss changes due to the presence of graphene oxide, the release of acidic substances into the solution, and the pH reduction [37].

Figure 10 b shows the pH values of the SBF solution as a function of soaking time. As can be seen, most changes in pH occurred in the early days such that pH declined from 7.4 to 7.8 after 3 days. The pH variation is due to the breakdown of



**Fig. 8** FESEM and elemental mapping of apatite formation on **a** HT and **b** HT-1GO scaffolds immersed in SBF for 14 days in static conditions



Si-O-Si bonds, the release of calcium and zinc ions in the SBF solution resulting in the formation of hydroxyl group silanol, and the creation of a negative charge over the surface of the sample. In the middle part, the surface adsorption of positively charged calcium ions occurred and led to a pH drop after about 8 days of immersion. Finally, negatively charged phosphate groups move toward the scaffold surface and led to the formation of the calcium phosphate (crystalline apatite or eventually amorphous) on the surface [76] and increasing the pH with a higher tangent. The pH of the SBF solution for a sample of HT containing 1 wt% GO in all times of soaking is lower than the pure HT ceramic but it is acceptable for in vitro bone cell culture application.

According to the MTT results (Fig. 11a), no toxicity was found for the scaffold specimens. HT-1GO samples showed more cell viability than HT samples, probably due to the graphene oxide’s higher surface area providing the radical groups for cell adhesion. Moreover, GO is polar and its negatively charged surface is coated with oxygen functional groups. The polar portion of a biological substance is reported with major impacts on the osteoblast cells’ biological activity since it enhances the cell-biological interaction of materials via polar forces [77]. This phenomenon indicates the synergistic effect of GO on improving cell viability. The viability of cells in this study was better than calcium silicate and apatites produced by freeze-cast method [78].

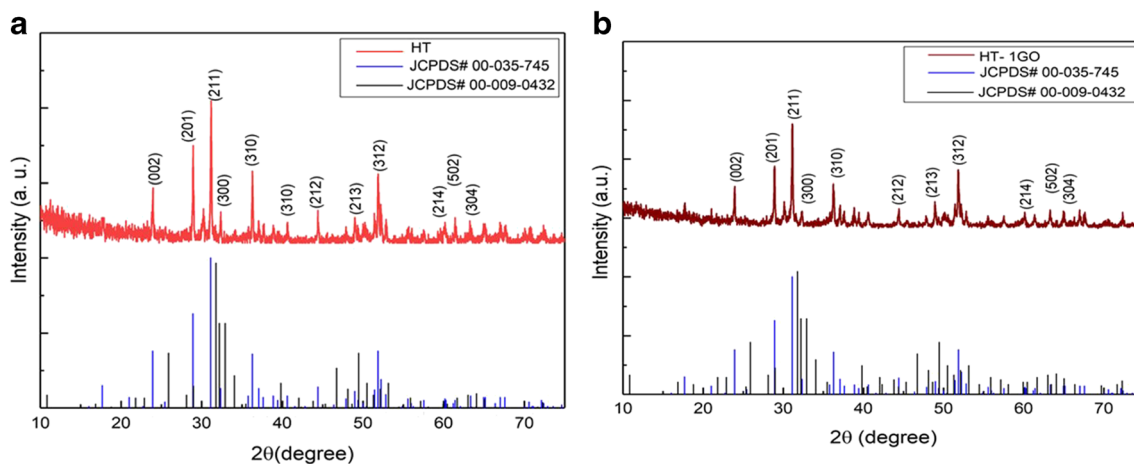


**Fig. 9** XRD of **a** HT and **b** HT-1GO samples after soaking in SBF for 14 days in static conditions

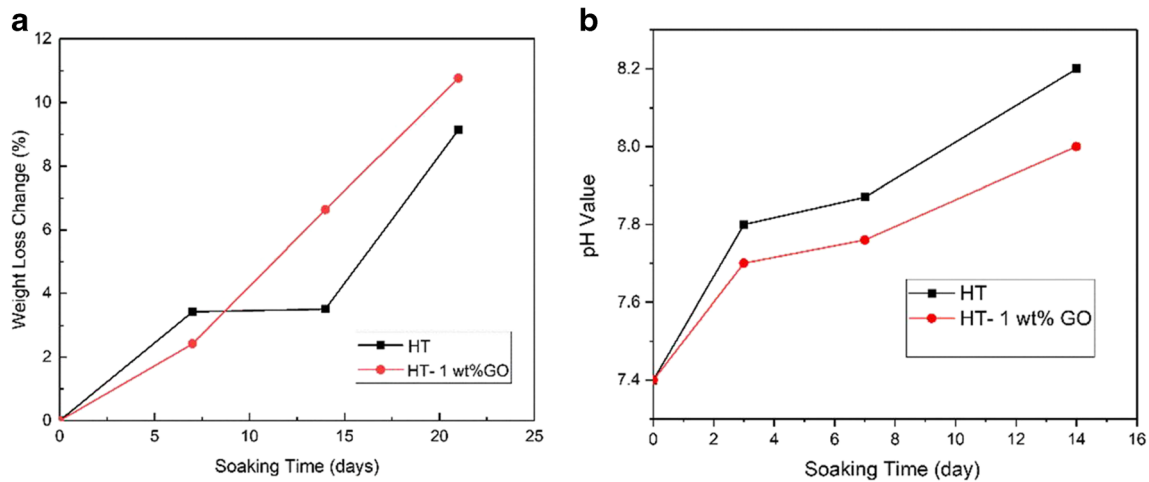
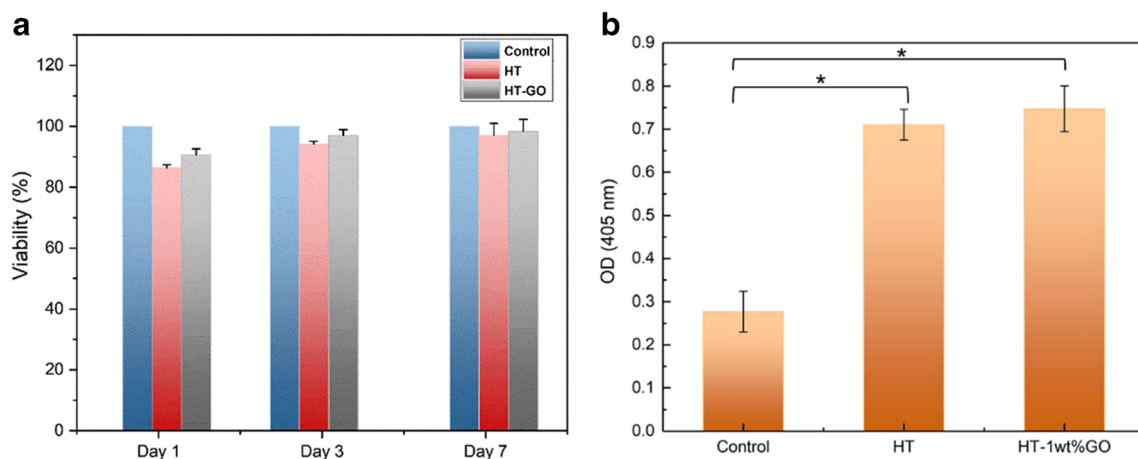


**Fig. 10** **a** Weight loss change of HT and HT-1GO samples in PBS solution for 21 days in static conditions. **b** pH value of HT and HT-1GO samples in the SBF solution after soaking for various durations

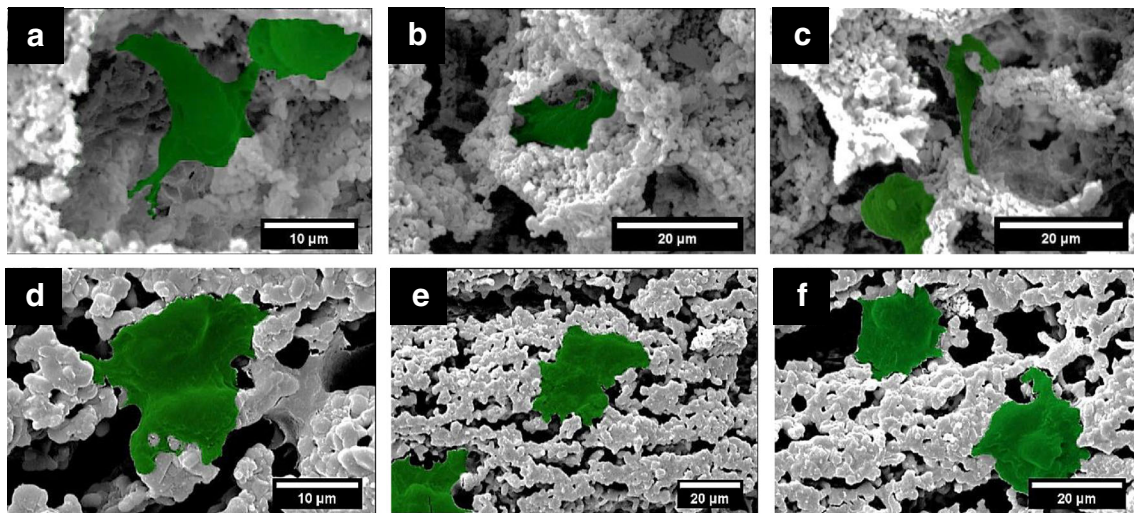
To assess the osteogenic differentiation of the MG-63 cells, an ALP test was performed on HT and HT-1GO samples. ALP is a bone activity marker that is expressed during osteogenesis. Cells in a culture medium without scaffold were considered the control group. ALP activity of MG 63 osteoblast cells after cultivation on HT and HT-1GO for 10 days is represented in Fig. 11b. Tukey's test was used to analyze the variance of cell viability and ALP results ( $p$ -value < 0.05). According to the results, the ALP activity of the HT and HT-1GO samples is significantly higher than the control condition, confirming the osteogenic differentiation of the cultured cells in the presence of HT and HT-1GO samples. GO can absorb proteins and other biomolecules and provide adhered cells with a local supply of chemical growth factors. Also, it enhances osteogenesis mineralization of the cells because of improving the nucleation of HA [79]. Therefore, ALP activity for a sample containing GO is higher than that of the pure sample and also previous works [78].

Figure 12 presents the morphology of the osteoblast cell adhesion onto the surface of HT and HT-1GO scaffolds cultured for 3 days. In HT-1GO scaffolds, compared to HT scaffolds, cells spread better and leave the spherical form. Material surface properties including the roughness, charge, softness, hydrophobicity, and chemical composition of the biomaterial surface have a strong effect on cell adhesion and growth, which are of great importance in the bone differentiation of cells in the body. GO with high in-plane stiffness, high surface energy, and amphiphilicity through bonded oxygen groups have various biomedical applications, particularly for cell growth performance. The bonded carbonyl, hydroxyl, carboxylate, and carboxyl groups over the graphene surface increase the interaction with proteins via hydrogen, covalent, electrostatic, and bonding. Hence, cell adhesion is improved by the increase in the protein content of the GO surface [80, 81].

The favorable surface properties of graphene-based substances can be a platform for osteoporosis and other tissue



**Fig. 11** **a** MTT assay of the cytotoxicity of the HT and HT-1GO samples for 1, 3, and 7 days. **b** ALP activity of MG63 osteoblast cells after cultivation on HT and HT-1GO for 10 days (data labeled with “\*” show a significant difference ( $P < 0.05$ )).



**Fig. 12** FESEM illustrating the morphology of MG63 osteoblast cells seeded on **a, b, and c** HT and **d, e, and f** HT-1GO composites after 72 h

engineering applications. Overall, the findings of the current study indicate that GO has adequate biocompatibility for using as a biomaterial, and adding GO into the HT matrix significantly improves the cellular response to the HT scaffold.

## Conclusion

In this study, the effects of GO nanosheets on physical, mechanical, bioactivity, and biocompatibility features of freeze-casted hardystonite scaffolds were investigated. Based on the results, the best mechanical features were obtained for the hardystonite-1 wt% GO ( $E = 71.77 \pm 2.40$  MPa,  $\sigma = 1.8 \pm 0.16$  MPa, and  $K = 47.87$  MJ/m<sup>3</sup>). FTIR, XRD, TGA, and SEM methods were used to characterize the scaffolds' features. The presence of GO increased the porosity and decreased the relative density of composite scaffolds compared to the HT scaffold. The HT-1GO scaffold as the optimum sample regarding mechanical properties showed excellent adhesion and proliferation of the osteoblastic cell. Besides, good bioactivity of the HT-1GO scaffold could be proven by bioactivity investigations in SBF under static conditions. Higher ability to cell viability and adsorb protein of HT-1GO indicated that the scaffold could be of high potential for use in bone tissue engineering.

**Funding** The authors would like to extend their gratitude for the financial supports provided by Iran National Science Foundation (INSF: Iran-Tehran, 98/6220/, Date: 20 April 2019) and Materials and Energy Research Center (MERC) with research grant (No.: 781397001).

## Declarations

**Competing interests** The authors declare no competing interests.

## References

- Burg, K.J.L., Porter, S., Kellam, J.F.: Biomaterial developments for bone tissue engineering. *Biomaterials*. **21**, 2347–2359 (2000). [https://doi.org/10.1016/S0142-9612\(00\)00102-2](https://doi.org/10.1016/S0142-9612(00)00102-2)
- Dinescu, S., Ionita, M., Ignat, S.R., Costache, M., Hermenean, A.: Graphene oxide enhances chitosan-based 3D scaffold properties for bone tissue engineering. *Int. J. Mol. Sci.* **20**, 5077 (2019). <https://doi.org/10.3390/ijms20205077>
- Shirtliff, V.J., Hench, L.L.: Bioactive materials for tissue engineering regeneration and repair. *Mater. Sci.* **38**, 4697–4707 (2003). <https://doi.org/10.1023/A:1027414700111>
- Shao, G., Hanaor, D.A.H., Shen, X., Gurlo, A.: Freeze casting: from low-dimensional building blocks to aligned porous structures—a review of novel materials, methods, and applications. *Adv. Mater.* **32**, 1907–1176 (2020). <https://doi.org/10.1002/adma.201907176>
- Schardosim, M., Soulié, J., Poquillon, D., Cazalbec, S., Duployer, B., Tenailleau, C., Rey, C., Hübler, R., Combes, C.: Freeze-casting for PLGA/carbonated apatite composite scaffolds: structure and properties. *Mater. Sci. Eng. C*. **77**, 731–738 (2017). <https://doi.org/10.1016/j.msec.2017.03.302>
- Le Huec, J.C., Schaefferbeke, T., Clement, D., Faber, J., Le Rebellier, A.: Influence of porosity on the mechanical resistance of hydroxyapatite ceramics under compressive stress. *Biomaterials*. **16**, 113–118 (1995). [https://doi.org/10.1016/0142-9612\(95\)98272-G](https://doi.org/10.1016/0142-9612(95)98272-G)
- Wegst, U.G., Schecter, M., Donius, A.E., Hunger, P.M.: Biomaterials by freeze casting. *Philos. Trans. R. Soc. London. Ser. A*. **368**, 2099–2121 (2010). <https://doi.org/10.1098/rsta.2010.0014>
- Huang, J., Rubink, W.S., Lide, H., Scharf, T.W., Banerjee, R., Jolandan, M.M.: Alumina-nickel composite processed via co-assembly using freeze-casting and Spark plasma Sintering. *Adv. Eng. Mater.* 1801103 (2018). <https://doi.org/10.1002/adem.201801103>
- Yang, Y., He, F., Ye, J.: Preparation, mechanical property and cytocompatibility of freeze-cast porous calcium phosphate ceramics reinforced by phosphate-based glass. *Mater. Sci. Eng. C*. **69**, 1004–1009 (2016). <https://doi.org/10.1016/j.msec.2016.08.008>
- Deville, S., Maire, E., Lasalle, A., Bogner, A., Gauthier, C., Leloup, J., et al.: Influence of particle size on ice nucleation and growth during the ice-templating process. *J. Am. Ceram. Soc.* **93**, 2507–2510 (2010). <https://doi.org/10.1111/j.1551-2916.2010.03840.x>

11. Lasalle, A., Guizard, C., Leloup, J., Deville, S., Maire, E., Bogner, A., et al.: Ice-templating of alumina suspensions: effect of supercooling and crystal growth during the initial freezing regime. *J. Am. Ceram. Soc.* **95**, 799–804 (2012). <https://doi.org/10.1111/j.1551-2916.2011.04993.x>
12. Zamanian, A., Farhangdoust, S., Yasaei, M., Khorami, M., Hafezi, M.: The effect of particle size on the mechanical and microstructural properties of freeze-casted macroporous hydroxyapatite scaffolds. *Int. J. Appl. Ceram. Technol.* **11**, 12–21 (2013). <https://doi.org/10.1111/ijac.12031>
13. Ye, F., Zhang, J., Liu, L., Zhan, H.: Effect of solid content on pore structure and mechanical properties of porous silicon nitride ceramics produced by freeze casting. *Mater. Sci. Eng. A.* **528**, 1421–1424 (2011). <https://doi.org/10.1016/J.MSEA.2010.10.066>
14. Deville, S.: Freeze-casting of porous ceramics: a review of current achievements and issues. *Adv. Eng. Mater.* **10**, 155–169 (2008). <https://doi.org/10.1002/adem.200700270>
15. Huang, T.H., Huang, T.H., Lin, Y.S., Chang, C.H., Chen, P.Y., Chang, S.W., Chen, C.S.: Phase-field modeling of microstructural evolution by freeze-casting. *Adv. Eng. Mater.* **00**, 1700343 (2017). <https://doi.org/10.1002/adem.201700343>
16. Farhangdoust, S., Zamanian, A., Yasaei, M., Khorami, M.: The effect of processing parameters and solid concentration on the mechanical and microstructural properties of freeze-casted macroporous hydroxyapatite scaffolds. *Mater. Sci. Eng. C.* **33**, 453–460 (2013). <https://doi.org/10.1016/j.msec.2012.09.013>
17. Deville, S., Saiz, E., Tomsia, A.P.: Ice-templated porous alumina structures. *Acta Mater.* **55**, 1965–1974 (2007). <https://doi.org/10.1016/j.actamat.2006.11.003>
18. Deville, S., Saiz, E., Tomsia, A.P.: Freeze casting of hydroxyapatite scaffolds for bone tissue engineering. *Biomaterials.* **27**, 5480–5490 (2006). <https://doi.org/10.1016/j.biomaterials.2006.06.028>
19. Sadeghzade, S., Emadi, R., Ghomi, H.: Mechanical alloying synthesis of forsteritediopside nanocomposite powder for using in tissue engineering. *Ceramics-Silikáty.* **59**, 1–5 (2015)
20. Hafezi, M., Nezafati, N., Nademehzad, A., Ghazanfari, S.M.H., Sepantamehr, M.: Bioinorganics in bioactive calcium silicate ceramics for bone tissue repair: bioactivity and biological properties. *Ceram. Sci. Technol.* **5**, 1–12 (2014). <https://doi.org/10.4416/JCST2013-00027>
21. Sadeghzade, S., Emadi, R., Tavangarian, F.: Combustion assisted synthesis of hardystonite nanopowder. *Ceram. Inter.* **42**, 14656–14660 (2016). <https://doi.org/10.1016/j.ceramint.2016.06.088>
22. Wu, C., Ramaswamy, Y., Zreiqat, H.: Porous Diopside (CaMgSi<sub>2</sub>O<sub>6</sub>) Scaffold: a promising bioactive material for bone tissue engineering. *Acta Biomater.* **6**, 2237–2245 (2010). <https://doi.org/10.1016/j.actbio.2009.12.022>
23. Geim, A.K., Novoselov, K.S.: The rise of graphene. *Nat. Mater.* **6**, 183–191 (2007). <https://doi.org/10.1038/nmat1849>
24. Kakran, M., Li, L.: Carbon nanomaterials for drug delivery. *Key. Eng. Mater.* **508**, 76–80 (2012). <https://doi.org/10.4028/www.scientific.net/KEM.508.76>
25. Shen, H., Zhang, L., Liu, M., Zhang, Z.: Biomedical applications of graphene. *Theranostics.* **2**, 283–294 (2012). <https://doi.org/10.7150/thno.3642>
26. Feng, L.Z., Liu, Z.A.: Graphene in biomedicine: opportunities and challenges. *Nanomedicine.* **6**, 317–324 (2011). <https://doi.org/10.2217/nmm.10.158>
27. Pan, Y., Sahoo, N.G., Li, L.: The application of graphene oxide in drug delivery. *Exp. Opin. Drug. Deliv.* **9**, 13265–13276 (2012). <https://doi.org/10.1517/17425247.2012.729575>
28. Liu, Z., Robinson, J.T., Tabakman, S.M., Yang, K., Dai, H.J.: Carbon materials for drug delivery & cancer therapy. *Mater. Today.* **14**, 316–323 (2011). [https://doi.org/10.1016/S1369-7021\(11\)70161-4](https://doi.org/10.1016/S1369-7021(11)70161-4)
29. Ghosh, D., Chandra, S., Chakraborty, A., Ghosh, S.K., Pramanik, P.: A novel graphene oxide-para amino benzoic acid nanosheet as effective drug delivery system to treat drug resistant bacteria. *Int. J. Pharm. Sci. Drug. Res.* **2**, 127–133 (2010). <https://ijpsdr.com/index.php/ijpsdr/article/view/103>
30. Walker, L.S., Marotto, V.R., Rafiee, M.A., Koratkar, N., Corral, E.L.: Toughening in graphene ceramic composites. *ACS. Nano.* **5**, 3182–3190 (2011). <https://doi.org/10.1021/nn200319d>
31. Bódis, E., Tapasztó, O., Károly, Z., Fazekas, P., Klébert, S., Mária Keszler, A., et al.: Spark plasma sintering of Si<sub>3</sub>N<sub>4</sub>/multilayer graphene composites. *Open. Chem.* **13**, 484–489 (2015). <https://doi.org/10.1515/chem-2015-0064>
32. Kuşoğlu, I.M., Çavdar, U., Altıntaş, A.: The effects of graphene nanoplatelet addition to in situ compacted alumina nanocomposites using ultra-high frequency induction sintering system. *J. Aust. Ceram. Soc.* **56**, 233–241 (2020). <https://doi.org/10.1007/s41779-019-00356-0>
33. Liu, Y., Huang, J., Li, H.: Synthesis of hydroxyapatite-reduced graphite oxide nanocomposites for biomedical applications: oriented nucleation and epitaxial growth of hydroxyapatite. *Mater. Chem. B.* **1**, 1826–1834 (2013). <https://doi.org/10.1039/C3TB00531C>
34. Liu, Y., Huang, J., Li, H.: Nanostructural characteristics of vacuum cold-sprayed hydroxyapatite/graphene-nanosheet coatings for biomedical applications. *Therm. Spray. Technol.* **23**, 1149–1156 (2014). <https://doi.org/10.1007/s11666-014-0069-2>
35. Gao, C., Liu, T., Shuai, C., Peng, S.: Enhancement mechanisms of graphene in nano-58S bioactive glass scaffold: mechanical and biological performance. *Sci. Rep.* **16**, 4712–4722 (2012). <https://doi.org/10.1038/srep04712>
36. Fan, Z., Wang, J., Liu, F., Nie, Y., Ren, L., Liu, B.: A new composite scaffold of bioactive glass nanoparticles/graphene: synchronous improvements of cytocompatibility and mechanical property. *Colloids. Surf. B.* **145**, 438–446 (2016). <https://doi.org/10.1038/srep0471210.1016/j.colsurfb.2016.05.026>
37. Mehrali, M., Moghaddam, E., Shirazi, S.F.S., Baradaran, S., Mehrali, M., Latibari, S.T., et al.: Synthesis, mechanical properties, and in vitro biocompatibility with osteoblasts of calcium silicate-reduced graphene oxide composites. *ACS. Appl. Mater. Inter.* **6**, 3947–3962 (2014). <https://doi.org/10.1021/am500845x>
38. Stankovich, S., Dikin, D.A., Dommett, G.H.B., et al.: Graphene-based composite materials. *Nature.* **442**, 282–286 (2006). <https://doi.org/10.1038/nature04969>
39. Williamson, G.K., Hall, W.H.: X-ray line broadening from filed aluminium and wolframL'elargissement des raies de rayons x obtenues des limailles d'aluminium et de tungsteneDie verbreiterung der roentgeninterferenzlinien von aluminium- und wolframspaenen. *Acta Metall.* **1**, 22–31 (1953)
40. Mallick, K.K.: Freeze casting of porous bioactive glass and bioceramics. *Am. Ceram. Soc.* **92**, 85–94 (2009). <https://doi.org/10.1111/j.1551-2916.2008.02784.x>
41. Heunisch, A., Dellert, A., Roosen, A.: Effect of powder, binder and process parameters on anisotropic shrinkage in tape cast ceramic products. *Eur. Ceram. Soc.* **30**, 3397–3406 (2010). <https://doi.org/10.1016/j.jeurceramsoc.2010.08.012>
42. Kokubo, T., Kushitani, H., Sakka, S., Kitsugi, T., Yamamuro, T.: Solutions able to reproduce in vivo surface-structure changes in bioactive glass-ceramic A-W3. *Biomed. Mater. Res.* **24**, 721–734 (1990). <https://doi.org/10.1002/jbm.820240607>
43. Depan, D., Misra, R.: The interplay between nanostructured carbon-grafted chitosan scaffolds and protein adsorption on the cellular response of osteoblasts: structure–function property relationship. *Acta Biomater.* **9**, 6084–6094 (2013). <https://doi.org/10.1016/j.actbio.2012.12.019>
44. Bazargan, A.M.: Sharif, F., Mazinani, S., Naderi, N.: Highly conductive reduced graphene oxide transparent ultrathin film through

- joule-heat induced direct reduction. *J Mater Sci: Mater Electron*. **28**, 1–9 (2017). <https://doi.org/10.1007/s10854-016-5676-x>
45. Farzin, A., Emadi, R., Fathi, M.H.: Novel Sol-gel-derived Hardystonite-based biomagnetic nanoparticles for hyperthermia applications. *J. Sol-Gel Sci. Technol.* **80**, 402–501 (2016). <https://doi.org/10.1007/s10971-016-4100-6>
  46. Bagherpour, I., Naghib, S.M., Yaghtin, A.H.: Synthesis and characterisation of nanostructured hardystonite coating on stainless steel for biomedical application. *IET Nanobiotechnol.* **12**, 895–902 (2018). <https://doi.org/10.1049/iet-nbt.2017.0275>
  47. Cacciotti, I., Lombardi, M., Bianco, A., Ravaglioli, A., Montanaro, L.: Sol-gel derived 45S5 bioglass: synthesis, microstructural evolution and thermal behavior. *Mater. Sci. Mater. Med.* **23**, 1849–1866 (2012). <https://doi.org/10.1007/s10856-012-4667-6>
  48. Aghajani, B., Karamian, E., Hosseini, B.: Hydroxyapatite-hardystonite nanocomposite scaffolds prepared by the replacing the polyurethane polymeric sponge technique for tissue engineering applications. *Nanomed.* **4**, 254–262 (2017). <https://doi.org/10.22038/nmj.2017.04.008>
  49. Mohammadi, H., Hafezi, M., Hesaraki, S., Sepantafar, M.M.: Preparation and characterization of Sr-Ti-hardystonite (Sr-Ti-HT) nanocomposite for bone repair application. *Nanomed.* **2**, 203–210 (2015). <https://doi.org/10.7508/nmj>
  50. Marcano, D.C., Kosynkin, D.V., Berlin, J.M., Sinitskii, A., Sun, Z., Slesarev, A., et al.: Improved synthesis of graphene oxide. *ACS Nano*. **4**, 4806–4814 (2010). <https://doi.org/10.1021/nn1006368>
  51. Xu, Y., Bai, H., Lu, G., Li, C., Shi, G.: Flexible graphene films via the filtration of water-soluble noncovalent functionalized graphene sheets. *Am. Chem. Soc.* **130**, 5856–5857 (2008). <https://doi.org/10.1021/ja800745y>
  52. Verma, S., Mungse, H.P., Kuma, N., Choudhary, S., Jain, S.L., Sain, B., et al.: Graphene oxide: an efficient and reusable carbocatalyst for aza-Michael addition of amines to activated alkenes. *Chem. Commun.* **47**, 12673–12675 (2011). <https://doi.org/10.1039/c1cc15230k>
  53. Asgarian, R., Doost-Mohammadi, A.: Evaluation of corrosion behavior, bioactivity and cytotoxicity of nanostructured hardystonite coating on Ti-6Al-4V substrate. *Surf. J.* **28**, 99–110 (2016)
  54. Wu, C., Chang, J., Zhai, W.: A novel hardystonite bioceramic: preparation and characteristics. *Ceram. Int.* **31**, 27–31 (2005). <https://doi.org/10.1016/j.ceramint.2004.02.008>
  55. Carter, C.B., Norton, M.G.: *Ceramic Materials: Science and Engineering*. Springer Science & Business Media, New York (2007)
  56. Yang, H., Xu, S., Jiang, L., Dan, Y.: Thermal decomposition behavior of poly (vinyl alcohol) with different hydroxyl content. *J. Macromol. Sci. Part B: Phys.* **51**, 464–480 (2012). <https://doi.org/10.1080/00222348.2011.597687>
  57. Hong, W., Meng, M., Xie, J., Gao, D., Xian, M., Wen, S., Huang, S., Kang, C.: Properties and thermal analysis study of modified polyvinyl acetate (PVA) adhesive. *J. Adh. Sci. Technol.* **32**, 2180–2194 (2018). <https://doi.org/10.1080/01694243.2018.1465687>
  58. Bai, R.G., Muthoosamy, K., Manickam, S., Alnaqbi, A.H.: Graphene-based 3D scaffolds in tissue engineering: fabrication, application, and future scope in liver tissue engineering. *Int. J. Nanomed.* **14**, 5753–5783 (2019). <https://doi.org/10.2147/IJN.S192779>
  59. Ege, D., Kamali, A.R., Boccaccini, A.R.: Graphene oxide/polymer-based biomaterials. *Adv. Eng. Mater.* **19**, 1700627 (2017). <https://doi.org/10.1002/adem.201700627>
  60. Maca, K., Pouchly, V., Zalud, P.: Two-step sintering of oxide ceramics with various crystal structures. *Eur. Ceram. Soc.* **30**, 583–589 (2010). <https://doi.org/10.1016/j.jeurceramsoc.2009.06.008>
  61. Barr, S.A., Luijten, E.: Structural properties of materials created through freeze casting. *Acta Mater.* **58**, 709–715 (2010). <https://doi.org/10.1016/j.actamat.2009.09.050>
  62. Dinescu, S., Ionita, M., Pandele, A.M., Galateanu, B., Iovu, H., Ardelean, A., Costache, M., Hermenean, A.: In vitro cytocompatibility evaluation of chitosan/graphene oxide 3D scaffold composites designed for bone tissue engineering. *Bio-Med. Mater. Eng.* **24**, 2249 (2014). <https://doi.org/10.3233/BME-141037>
  63. Nair, M., Nancy, D., Krishnan, A.G., Anjusree, G.S., Vadukumpully, S., Nair, S.V.: Graphene oxide nanoflakes incorporated gelatin-hydroxyapatite scaffolds enhance osteogenic differentiation of human mesenchymal stem cell. *Nanotechnol.* **26**, 161001–161011 (2015). <https://doi.org/10.1088/0957-4484/26/16/161001>
  64. Munch, E., Launey, M.E., Alsem, D.H., Saiz, E., Tomsia, A.P., Ritchie, R.O.: Tough, bio-inspired hybrid materials. *Science*. **322**, 1516–1520 (2008). <https://doi.org/10.1126/science.1164865>
  65. Raucci, M.G., Giugliano, D., Longo, A., Zeppetelli, S., Carotenuto, G., Ambrosio, L.: Comparative facile methods for preparing graphene oxide–hydroxyapatite for bone tissue engineering. *Tissue. Eng. Reg. Med.* **11**, 2204–2216 (2016). <https://doi.org/10.1002/term.2119>
  66. Gao, C., Liu, T., Shuai, C., Peng, S.: Enhancement mechanisms of graphene in nano-58S bioactive glass scaffold: mechanical and biological performance. *Sci. Rep.* **4**, 4712–4722 (2014). <https://doi.org/10.1038/srep04712>
  67. Liu, J., Yang, Y., Hasssinin, H., Jumbu, N., Deng, S., Zuo, Q., Jiang, K.: Graphene-alumina nanocomposites with improved mechanical properties for biomedical applications. *ACS Appl. Mater. Interfaces.* **8**, 2607–2616 (2016). <https://doi.org/10.1021/acsami.5b10424>
  68. Liu, X., Fan, Y.C., Li, J.L., Wang, L.J., Jiang, W.: Preparation and mechanical properties of graphene nanosheet reinforced alumina composites. *Adv. Eng. Mater.* **17**, 28–35 (2015). <https://doi.org/10.1002/adem.201400231>
  69. Ghzanfari, S.M.H., Zamanian, A.: Phase transformation, microstructural and mechanical properties of hydroxyapatite/alumina nanocomposite scaffolds produced by freeze casting. *Ceram. Inter.* **39**, 9835–9844 (2013). <https://doi.org/10.1016/j.ceramint.2013.05.096>
  70. Sadeghpour, S., Amirjani, A.M., Hafezi, M., Zamanian, A.: Fabrication of a novel nanostructured calcium zirconium silicate scaffolds prepared by a freeze-casting method for bone tissue engineering. *Ceram. Inter.* **40**, 16107–16114 (2014). <https://doi.org/10.1016/j.ceramint.2014.07.039>
  71. Hafezi, M., Nezafati, N., Ali Nadernezhad, A., Yasaei, M., Zamanian, A., Mobini, S.: Effect of sintering temperature and cooling rate on the morphology, mechanical behavior and apatite-forming ability of a novel nanostructured magnesium calcium silicate scaffold prepared by a freeze casting method. *J. Mater. Sci.* **49**, 1297–1305 (2014). <https://doi.org/10.1007/s10853-013-7813-8>
  72. Shahbazi, M.A., Ghalkhani, M., Maleki, H.: Directional freeze-casting: a bioinspired method to assemble multifunctional aligned porous structures for advanced applications. *Adv. Eng. Mater.* 2000033–2000059 (2020). <https://doi.org/10.1002/adem.202000033>
  73. Baradaran, S.: Mechanical and biological evaluations of hydroxyapatite composite for orthopedic applications. Ph.D. degree, University of Malaya, Kuala Lumpur, (2015).
  74. Depan, D., Pesacreata, T., Misra, R.: The synergistic effect of a hybrid graphene oxide-chitosan system and biomimetic mineralization on osteoblast function. *Biomater. Sci.* **2**, 264–274 (2014). <https://doi.org/10.1039/C3BM60192G>
  75. Wan, C., Chen, B.: Poly (ε-Caprolactone)/graphene oxide biocomposites: mechanical properties and bioactivity. *Biomed.*

- Mater. **6**, 055010 (2011). <https://doi.org/10.1088/1748-6041/6/5/055010>
76. Chengtie, W.U., Chang, J., Zhai, W., Ni, S.: A novel bioactive porous bredigite ( $\text{Ca}_7\text{MgSi}_4\text{O}_{16}$ ) scaffold with biomimetic apatite layer for bone tissue engineering. *Mater. Sci: Mater. Med.* **18**, 857–864 (2007). <https://doi.org/10.1007/s10856-006-0083-0>
77. Olada, A., Bakht Khosh Hagha, H., Mirmohsenia, A., Farshi Azharb, F.: Graphene oxide and montmorillonite enriched natural polymeric scaffold for bone tissue engineering. *Ceram. Inter.* **45**, 15609–15619 (2019). <https://doi.org/10.1016/j.ceramint.2019.05.071>
78. Qiang, F.U.: Freeze casting of bioactive glass and ceramic scaffolds for bone tissue engineering. Ph.D. degree. Faculty of the Graduate School of the Missouri university of science and technology. (2009)
79. Nasrollahi, N., Dehkordi, A.N., Jamshidizad, A., Chehelgerdi, M.: Preparation of brushite cements with improved properties by adding graphene oxide. *Int. J. Nanomed.* **14**, 3785–3797 (2019). <https://doi.org/10.2147/IJN.S196666>
80. Jeong, J.T., Choi, M.K., Sim, Y., Lim, J.T., Kim, G.S., Seong, M.J., Hyung, J.H., Kim, K.S., Umar, A., Lee, S.K.: Effect of graphene oxide ratio on the cell adhesion and growth behavior on a graphene oxide-coated silicon substrate. *Sci. Rep.* **6**, 33835–33845 (2016). <https://doi.org/10.1038/srep33835>
81. Eberli, D.: Regenerative medicine and tissue engineering-cells and biomaterials, pp. 569–588. In *Tech* (2011)

**Publisher's note** Springer Nature remains neutral with regard to jurisdictional claims in published maps and institutional affiliations.